Lattice dynamics and spin-phonon coupling in $CaMn_2O_4$: A Raman study

V. G. Ivanov,[1] V. G. Hadjiev,[2] A. P. Litvinchuk,[2] D. Z. Dimitrov,[3] B. L. Shivachev,[4] M. V. Abrashev,[1,5] B. Lorenz,[2] and M. N. Iliev[2]

[1]*Faculty of Physics, University of Sofia, 1164 Sofia, Bulgaria*
[2]*Texas Center for Superconductivity, University of Houston, Houston, Texas 77204-5002, USA*
[3]*Institute of Optical Materials and Technologies, Bulgarian Academy of Sciences, 1113 Sofia, Bulgaria*
[4]*Institute of Mineralogy and Crystallography, Bulgarian Academy of Sciences, 1113 Sofia, Bulgaria*
[5]*Instituto de Física, UFRGS, Porto Alegre, 91501-970 Rio Grande do Sul, Brazil*

(Received 12 March 2014; revised manuscript received 20 May 2014; published 30 May 2014)

We present polarized Raman spectra of $CaMn_2O_4$ (marokite) measured in several exact scattering configurations from oriented single crystals. Most of the $11A_g + 12B_{1g} + 10B_{2g} + 9B_{3g}$ Raman-allowed modes are identified and assigned to definite atomic motions by comparison to the predictions of *ab initio* lattice dynamical calculations. The Raman modes at 474 cm^{-1} (A_g), 478 cm^{-1} (B_{1g}), and 614 cm^{-1} (B_{1g}) exhibit anomalous softening at temperatures below $T_N \approx 220$ K due to a spin-phonon coupling which depends strongly on the phonon eigenvectors. There are no indications for a structural transition in the temperature range between 80 and 850 K. We argue quantitatively that the mechanism of the phonon softening below T_N is similar to that in the undoped manganese perovskites.

DOI: 10.1103/PhysRevB.89.184307 PACS number(s): 78.30.−j, 75.47.Lx, 75.30.Et

I. INTRODUCTION

Ternary manganese-based oxides, i.e., perovskites and spinels, attract considerable interest due to the strong correlation between their structural, magnetic, electrical, and optical properties. Doped perovskite manganites of a generic formula $RMnO_3$ (R = rare earth) have been extensively studied in the last two decades in the context of the colossal magnetoresistance (CMR) and orbital ordering phenomena. It has been widely accepted that the Jahn-Teller (JT) distortion of the local atomic environment of Mn^{3+} ions underlies the peculiar structural, magnetic, and transport properties of this class of compounds. On the other hand, manganese spinels, e.g., $LiMn_2O_4$, are promising environment-friendly materials for the fabrication of large-capacity Li-storage electrodes [1].

Another uncommon yet interesting ternary manganese oxide is the *marokite* $CaMn_2O_4$, which crystallizes in the orthorhombic $Pbcm$ symmetry [2], shown in the left panel of Fig. 1. The chemical composition of marokite corresponds to that of a spinel AB_2O_4 and, indeed, several spinels containing A ions of a relatively small radius transform into $Pbcm$ structure under high pressure [3,4]. In the case of $CaMn_2O_4$, the marokite structure is stable at ambient conditions due to the chemical pressure exerted by the large-radius Ca^{2+} ions. The manganese ions in $CaMn_2O_4$ are at a high-spin, $S = 2$, Mn^{3+} oxidation state, which possesses, for a large JT, distortion of the MnO_6 octahedra. The apical Mn-O bonds along the singly occupied Mn d_{z^2} orbitals are longer by ≈26% than the equatorial bonds. The compound undergoes an antiferromagnetic transition at a Néel temperature of $T_N \approx$ 220 K, as evidenced by magnetic susceptibility and neutron-diffraction (ND) measurements [5,6]. The antiferromagnetic transition results in a doubling of the unit cell along the crystallographic a axis and a spin alignment in the same direction.

The compound has attracted interest mainly for its magnetic properties [7,8], but recently transport and thermodynamic properties [8] have also been addressed experimentally. The optical absorption and the electronic band structure of $CaMn_2O_4$ have been studied in relation to its excellent photocatalytic properties [9].

The primary goal of our work is to characterize the optical phonons in $CaMn_2O_4$ by means of polarized Raman spectroscopy. This is an important task in several aspects. First, marokite has been observed as a low-level impurity phase in $Ca_{1-x}La_xMnO_3$, which interferes with the magnetic susceptibility and neutron-diffraction pattern of the dominant phase [5]. This raises the question of a reliable identification of marokite in a multiphase system. Raman spectroscopy has been proven as a powerful characterization technique, allowing for detection of phase inclusions on a micrometer scale. Wang *et al.* [3] reported nonpolarized Raman spectra of polycrystalline $CaMn_2O_4$ at ambient pressure and its changes under hydrostatic pressure up to 74 GPa. Unfortunately, due to a possible error in the symmetry analysis, they have expected a smaller number of Raman-active modes, namely, 24 ($6A_g + 7B_{1g} + 6B_{2g} + 5B_{3g}$) instead of 42 ($11A_g + 12B_{1g} + 10B_{2g} + 9B_{3g}$). In addition, the symmetry of experimentally observed lines has not been determined. Here we report polarized Raman spectra of $CaMn_2O_4$ obtained from single crystals in several exact scattering configurations, which allowed us to determine unequivocally the mode symmetries. All except for two of the expected Raman-active modes were identified and assigned to definite atomic motions by comparison to the predictions of lattice dynamical calculations (LDC).

Second, the large JT distortions in $CaMn_2O_4$ let us expect a spin-phonon coupling below T_N as strong as that observed in manganese perovskites [10–12]. That is why we performed detailed temperature-dependent Raman measurements and established a sizable frequency softening of some of the Raman-active modes below the antiferromagnetic transition temperature. This finding is discussed in the frame of the mechanism proposed by Granado *et al.* (Ref. [11]) for a qualitative explanation of the same effect in perovskite manganites. However, we proceed further and quantify the observed phonon softening by utilizing the molecular orbital dimer approach [13] to the superexchange interactions in $CaMn_2O_4$.

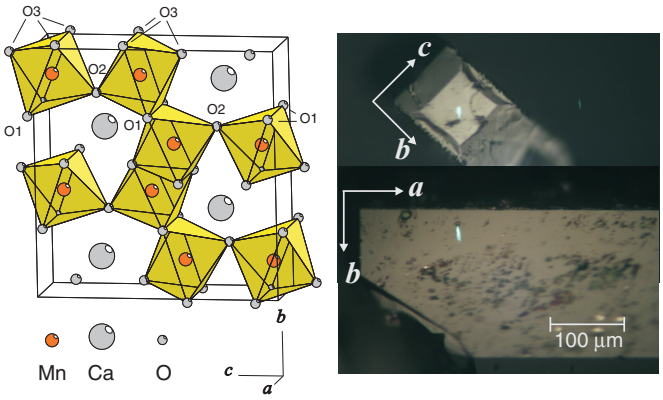

FIG. 1. (Color online) Unit cell of $CaMn_2O_4$ (space group No. 57 $Pbcm$, $Z = 4$).

The paper is organized as follows. In Sec. II, we describe the experimental procedure and the details of lattice dynamics calculations. Experimental results and their interpretation in the frame of symmetry analysis and LDC are presented in Sec. III. A quantitative model of the spin-phonon interaction is proposed in Sec. IV. The main conclusions of the work are formulated in Sec. V.

II. SAMPLES, EXPERIMENTAL AND CALCULATION DETAILS

$CaMn_2O_4$ single crystals were grown using the high-temperature solution growth method in pure platinum crucibles. $CaCl_2$ was used as flux and the ratio (in weight percents) between the starting products and the flux $(CaO + 2MnO_2)$:$CaCl_2$ was 1:20. The starting mixture was heated in air for 12 h at 1200 °C, and after that it was homogenized for 48 h. The $CaMn_2O_4$ crystal growth was accomplished during the cooling of the molten mixture in the temperature range from 1200 to 800 °C (cooling speed 3 °C/h). After that the crystals were cooled down to room temperature at a rate of 100 °C/h. The $CaMn_2O_4$ crystallized on the walls and the bottom of the platinum crucible in the form of elongated platelets of typical dimensions $1 \times 0.4 \times 0.05$ mm^3.

The crystal structure characterization of as-grown $CaMn_2O_4$ was performed by x-ray single-crystal analysis. The data were collected at room temperature on a Super Nova Dual (Agilent) diffractometer with Mo radiation ($\lambda = 0.07107\,3$ nm). The crystal structure was solved by direct methods and refined by the full matrix least-squares procedure on F^2 using the SHELXL-97 code [14]. The structure was found to belong to the orthorhombic space group $Pbcm$ with unit cell parameters $a = 3.1478(2)$Å, $b = 9.9750(6)$Å, and $c = 9.6647(7)$Å. The unit cell and some of the crystal surfaces used to obtain the polarized Raman spectra are shown in Fig. 1.

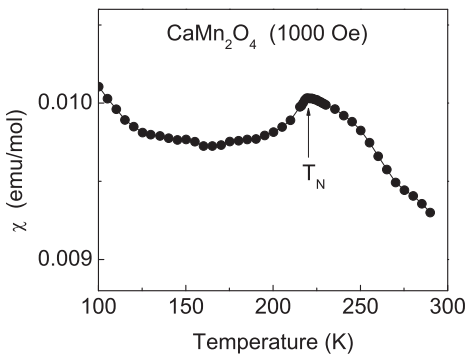

FIG. 2. Magnetic susceptibility of a bundle of randomly oriented $CaMn_2O_4$ crystals measured in an applied field of 1000 Oe.

The magnetic susceptibility $\chi(T)$ of a bundle of randomly oriented $CaMn_2O_4$ crystals was measured in an applied field of 1000 Oe by employing a superconducting quantum interference magnetometer (MPMS, Quantum Design). The antiferromagnetic (AFM) transition at $T_N = 220$ K is clear from the temperature dependence of the magnetic susceptibility shown in Fig. 2. The increase of χ at lower T attributed to the presence of small amount of Mn^{4+} ions is consistent with that of previous reports [5–8].

The Raman spectra were collected under microscope with 633, 515, and 488 nm excitation using a T64000 (Horiba-Jobin-Yvon) spectrometer. In low-temperature measurements, the samples were cooled in an Oxford Microstat^{He} cryostat, whereas for high-temperature measurements, a Linkam FIR600 heating stage was used. The room-temperature spectra were obtained in all informative backscattering configurations, namely, aa, bb, cc, ab, ac, and bc. In these notations, the first letter represents the polarization direction of the incident radiation, and the second one represents the polarization of the scattered light.

The lattice dynamics calculations were performed within the generalized-gradient approximation (GGA) of the density functional perturbation theory (DFPT) with Perdew-Burke-Ernzerhof (PBE) exchange-correlation functional, plane-wave basis, and norm-conserved pseudopotentials, as implemented in the QUANTUM ESPRESSO suite [15]. The electronic band structure, related properties, and geometry optimization of the crystal structure were calculated in a self-consistent field (SCF) with 50 Ry kinetic-energy cutoff for the plane waves, 200 Ry charge density cutoff, SCF tolerance better than 10^{-7}, and phonon SCF threshold of 10^{-12}. As expected, non-spin-polarized DFT calculations produce a metallic ground state due to the partially occupied Mn $3d$ shell in $CaMn_2O_4$. The compound, however, is an insulator [8] with an energy gap of 1.29 eV measured in the optical absorption experiments [9]. Calculations using the DFT+U approach with Hubbard on-site repulsion potential U for Mn ranging from 2.5 to 4.5 eV result in the opening of an energy gap of 0.5–0.8 eV in the band structure of $CaMn_2O_4$. The optical absorption calculations based on the DFT+U band structure, however, cannot reproduce the observed optical absorption edge [9]. The most reliable results concerning optical properties and lattice dynamics were obtained by means of spin-polarized (SP) DFT calculations. Two types of SP calculations were performed—on a single $Pbcm$ unit cell, resulting in a ferromagnetic (FM) state, and on a cell that was doubled along the a axis, reproducing the AFM spin alignment of Mn^{3+} ions. In both cases, however, a nonmetallic electronic band structure was found with energy gaps of 1.2 and 1.85 eV for the FM and AFM spin alignment, respectively.

The Raman-active phonons in $CaMn_2O_4$ were calculated for both the FM and AFM structures. The $\mathbf{k} = 0$ normal

TABLE I. Decomposition of the normal vibrations in $CaMn_2O_4$ into irreducible representations of the space group $Pbcm$ (No. 57) and selection rules for the Raman-active modes.

Atom	Wyckoff position	Mode decomposition by symmetry
Ca	4*d*	$2A_g + A_u + 2B_{1g} + B_{1u} + B_{2g} + 2B_{2u} + B_{3g} + 2B_{3u}$
Mn	8*e*	$3A_g + 3A_u + 3B_{1g} + 3B_{1u} + 3B_{2g} + 3B_{2u} + 3B_{3g} + 3B_{3u}$
O1	4*c*	$A_g + A_u + 2B_{1g} + 2B_{1u} + 2B_{2g} + 2B_{2u} + B_{3g} + B_{3u}$
O2	4*d*	$2A_g + A_u + 2B_{1g} + B_{1u} + B_{2g} + 2B_{2u} + B_{3g} + 2B_{3u}$
O3	8*e*	$3A_g + 3A_u + 3B_{1g} + 3B_{1u} + 3B_{2g} + 3B_{2u} + 3B_{3g} + 3B_{3u}$
Raman modes:		$11A_g + 12B_{1g} + 10B_{2g} + 9B_{3g}$
Selection rules:		$A_g(aa,bb,cc)$, $B_{1g}(ab)$, $B_{2g}(ac)$, $B_{3g}(bc)$

modes in the doubled AFM cell were projected onto Γ- and *X*-point representations of the single *Pbcm* cell. In this way, no differences in the number and the symmetry of Raman-active modes have been found between the AFM and FM structures. Most importantly for this work, the calculated eigenvectors of the Γ-point modes are similar for the AFM and FM structures, which allowed us to identify the atomic displacements responsible for the phonon anomalies in $CaMn_2O_4$ below T_N.

III. RESULTS AND DISCUSSION

Table I summarizes the decomposition of normal modes in $CaMn_2O_4$ by symmetry [16]. In total, 42 Raman-active modes ($11A_g + 12B_{1g} + 10B_{2g} + 9B_{3g}$) are expected for the *Pbcm* structure. The A_g modes are allowed in the parallel (*aa*, *bb*, *cc*) but forbidden in the crossed (*ab*, *ac*, *bc*) scattering configurations. In the experimentally accessible configurations, the B_{1g} modes are only allowed in *ab*, the B_{2g} modes are only allowable in *ac*, and the B_{3g} modes are only allowable in *bc*. Therefore, the comparison of the spectra obtained in all exact configurations allows for unambiguous assignment of the symmetry of the experimentally observed Raman lines.

The room-temperature polarized Raman spectra of $CaMn_2O_4$ are shown in Fig. 3. The observed spectral bands strictly follow the polarization selection rules of the Raman-active modes, as shown in Table I. The experimental frequencies are classified by symmetry in Table II and are compared to those predicted by the calculations of lattice dynamics.

As it follows from Table II, out of a total of 42 Raman-active modes, only one B_{1g} and one B_{2g} have not been detected. The absolute and relative intensities of the Raman lines, however, vary strongly with the excitation wavelength. This is illustrated in Fig. 4 where Raman spectra obtained with the same incident laser power of ≈1 mW but different excitation wavelengths of 633 nm (1.96 eV), 515 nm (2.41 eV), and 488 nm (2.54 eV) are compared. Note that the intensities of the 515 nm and 488 nm spectra are multiplied by factors of 5 and 20, respectively. The resonant enhancement of the A_g modes at 121, 376, and 632 cm^{-1} and B_{1g} modes at 120 and 614 cm^{-1} for a 633 nm excitation corroborates the optical absorption peak at 638 nm, which has been assigned to an O($2p\uparrow$)–Mn($e_g\uparrow$) electronic transition [9].

The temperature evolution of the *aa* (A_g) and *ab* (B_{1g}) Raman spectra was studied in details between 80 and 850 K. As it follows from Fig. 5, most of the Raman modes exhibit the expected hardening and narrowing upon decreasing the temperature. In the absence of a structural transition, the temperature variation of the mode frequency $\omega(T)$ is known to be primarily due to an anharmonic phonon decay [17,18] resulting in a functional dependence:

$$\omega(T) = \omega_0 - C\left(1 + \frac{2}{e^x - 1}\right), \quad (1)$$

where ω_0 is the phonon frequency in harmonic approximation, C is the anharmonic correction to the frequency at $T = 0$ K, and $x = \hbar\omega_0/2k_BT$.

This model describes adequately the temperature dependence of most of the phonon modes in $CaMn_2O_4$ for the whole temperature range between 80 and 850 K, as shown in the left panels of Fig. 6. The magnetic ordering below 220 K, however, results in an anomalous softening of three of the Raman modes, near 474 cm^{-1} [$A_g(9)$], 478 cm^{-1} [$B_{1g}(8)$], and 614 cm^{-1} [$B_{1g}(11)$], as evidenced in the right panels of Fig. 6. At 80 K, the frequency downshift of these modes is about 3 cm^{-1} relative to the corresponding frequencies at

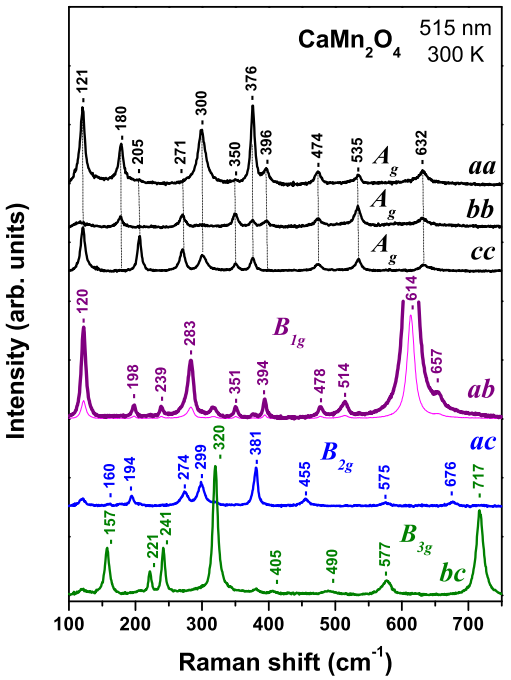

FIG. 3. (Color online) Raman spectra of $CaMn_2O_4$ as obtained at room temperature with 515 nm excitation.

TABLE II. Comparison of experimentally observed and LDC-predicted frequencies (in cm^{-1}) for the A_g, B_{1g}, B_{2g}, and B_{3g} modes in $CaMn_2O_4$. The columns AFM (FM) report the calculated mode frequencies for an antiferromagnetic (ferromagnetic) arrangement of Mn^{3+} spins.

Mode	Expt.	AFM	FM	Mode	Expt.	AFM	FM	Mode	Expt.	AFM	FM	Mode	Expt.	AFM	FM
$A_g(1)$	121	123	134	$B_{1g}(1)$	120	121	136	$B_{2g}(1)$	132	127	135	$B_{3g}(1)$	157	171	167
$A_g(2)$	180	155	177	$B_{1g}(2)$	198	185	173	$B_{2g}(2)$	160	171	166	$B_{3g}(2)$	221	217	219
$A_g(3)$	205	202	204	$B_{1g}(3)$	239	220	203	$B_{2g}(3)$	194	181	199	$B_{3g}(3)$	241	240	237
$A_g(4)$	271	277	305	$B_{1g}(4)$	283	252	243	$B_{2g}(4)$	274	282	273	$B_{3g}(4)$	285	306	309
$A_g(5)$	300	290	353	$B_{1g}(5)$	317	320	284	$B_{2g}(5)$	299	301	340	$B_{3g}(5)$	320	318	346
$A_g(6)$	350	313	386	$B_{1g}(6)$	351	366	371	$B_{2g}(6)$	381	354	371	$B_{3g}(6)$	405	394	422
$A_g(7)$	376	361	443	$B_{1g}(7)$	394	430	414	$B_{2g}(7)$	455	497	464	$B_{3g}(7)$	490	486	526
$A_g(8)$	396	390	479	$B_{1g}(8)$	478	496	433	$B_{2g}(8)$		548	552	$B_{3g}(8)$	577	560	589
$A_g(9)$	474	456	536	$B_{1g}(9)$	514	506	502	$B_{2g}(9)$	575	581	576	$B_{3g}(9)$	717	622	732
$A_g(10)$	535	530	598	$B_{1g}(10)$		546	561	$B_{2g}(10)$	676	586	702				
$A_g(11)$	632	604	662	$B_{1g}(11)$	614	588	566								
				$B_{1g}(12)$	657	617	683								

T_N, and nearly 5–6 cm^{-1} with respect to the low-temperature extrapolation of Eq. (1).

Figure 7 shows the calculated atomic displacements for the three modes exhibiting anomalous softening below T_N. The reported eigenvectors correspond to the spin-polarized calculations on a doubled AFM unit cell. However, qualitatively the same displacement pattern was obtained in the calculations on the crystallographic (FM) unit cell. The modes at these frequencies are comprised of almost pure oxygen vibrations with atomic motions within the planes of Mn-O-Mn bond angles. An exception is the O1 displacement in the $B_{1g}(8)$ mode, which has a small off-plane component. For the calculated $A_g(9)$ mode, the O1 atoms vibrate along the crystallographic *a* axis, but the displacement vector is not seen in the *bc* section of the unit cell in Fig 7. This motion, however, is also of in-plane character with respect to the Mn-O1-Mn bond angle.

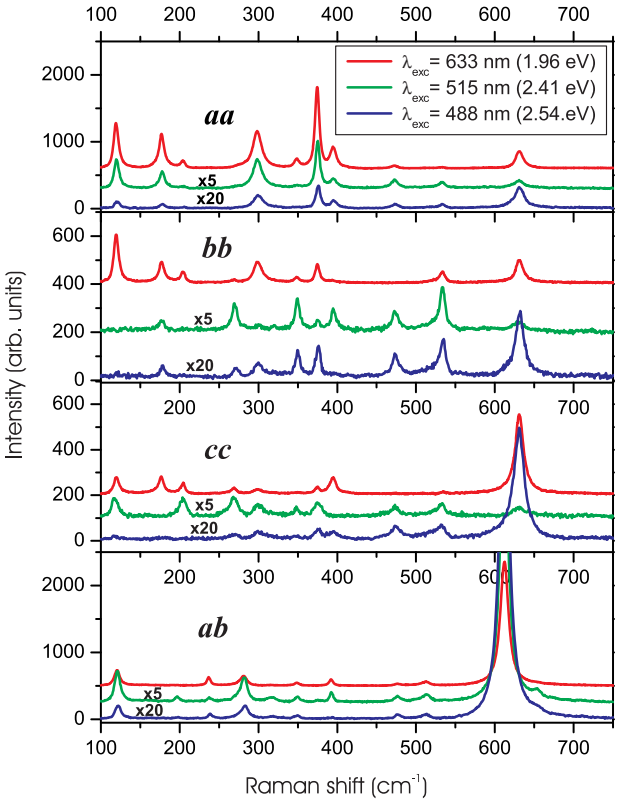

FIG. 4. (Color online) Comparison of $aa(A_g)$, $bb(A_g)$, $cc(A_g)$, and $ab(B_{1g})$ Raman spectra obtained with 633, 515, and 488 nm excitation. The intensities of the 515 nm and 488 nm spectra are multiplied by factors 5 and 20, respectively.

IV. MECHANISM OF THE PHONON RENORMALIZATION BELOW T_N

Phonon softening of a similar magnitude has been observed below T_N for the manganese perovskite $LaMnO_3$ [10,11] and later on in the whole series of orthorhombic $RMnO_3$ [12] (R = rare earth). Granado *et al.* [10] discussed different

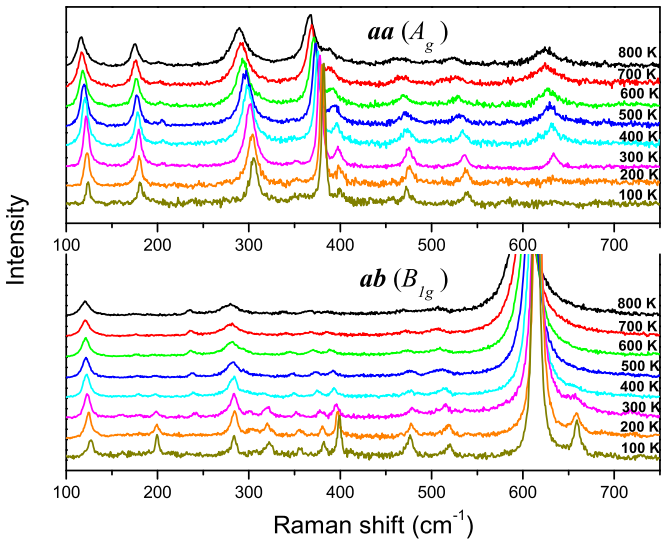

FIG. 5. (Color online) Temperature-dependent Raman spectra of $CaMn_2O_4$ as obtained with a 515 nm excitation between 100 and 800 K. The intensities of the *aa* and *ab* spectra are normalized, respectively, to the integrated intensity of the A_g mode near 380 cm^{-1} and B_{1g} mode near 614 cm^{-1}.

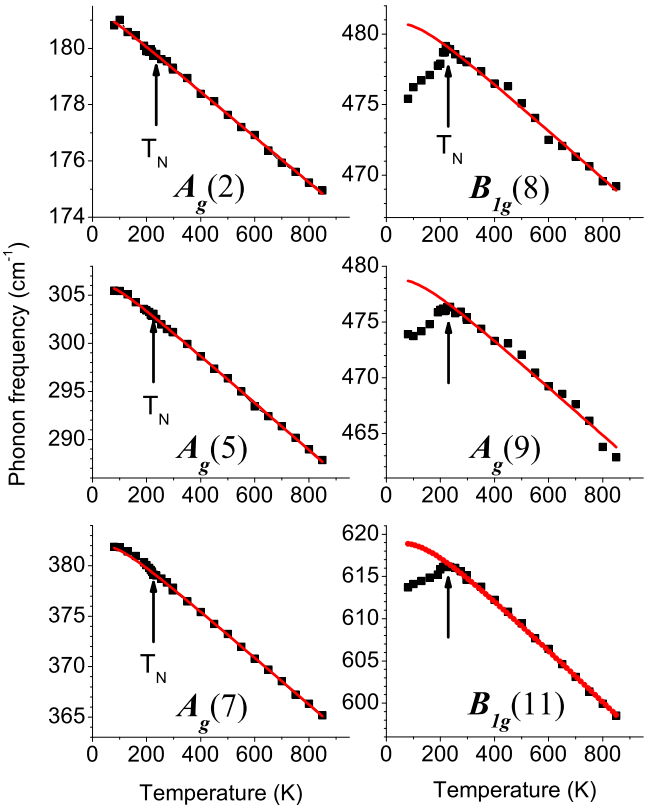

FIG. 6. (Color online) Temperature dependence of the frequency of Raman modes not affected (left column) and affected (right column) by the magnetic ordering below $T_N = 220$ K. The red lines represent the least-squares fit of the experimental data in the range 220–850 K following Eq. (1).

mechanisms, which may affect the phonon frequencies below the magnetic transition temperature, and came to the conclusion that the effect is primarily due to the dependence of the exchange integrals J between Mn^{3+} spins on the displacement of oxygen atoms mediating the magnetic superexchange. More concretely, they have derived a general formula for the frequency renormalization $\Delta\omega$ of an oxygen vibration due to magnetic ordering:

$$\Delta\omega = \frac{1}{2m\omega}\sum_j \frac{\partial^2 J_{ij}}{\partial u^2}\langle S_i \cdot S_j\rangle, \tag{2}$$

where m is the oxygen mass, ω is the unrenormalized mode frequency, u is the oxygen displacement about the equilibrium position, and J_{ij} and $\langle S_i \cdot S_j\rangle$ are, respectively, the exchange integral and the spin-spin correlation function for the Mn ions i and j. Hereafter, we will adopt the convention of assigning a positive/negative J to the antiferromagnetic/ferromagnetic (AFM/FM) exchange. If the exchange interactions are restricted to nearest neighbors only, then the spin-spin correlation function in Eq. (2) is negative in the case of AFM ordering. Consequently, the frequency softening implies a positive second derivative of the exchange integral with respect to the oxygen displacement. For temperatures well below T_N, the spin-spin correlation function is approximated as $\langle S_i \cdot S_j\rangle \approx -M^2$, where M is the static magnetization per Mn^{3+} ion in units of Bohr's magneton. As a support to the model described above, it has been demonstrated in Ref. [11] that at low temperatures, the phonon softening $\Delta\omega$ scales as the square of magnetization.

The fact that most of the Raman lines follow the standard anharmonic behavior below T_N signifies that the magnetostriction effects are not dominant in $CaMn_2O_4$. It is plausible, therefore, to assume that the mechanism of phonon anomalies in $CaMn_2O_4$ is similar to that in manganese perovskites. Being phenomenological, however, the model of Granado *et al.* does not prescribe a specific sign to the second derivative $\partial^2 J/\partial u^2$ and, correspondingly, does not predict the sign of the effect on the phonon frequency—softening or hardening. Therefore, in order to validate this mechanism in our case, we have to concentrate on the microscopic description of the superexchange interactions in $CaMn_2O_4$.

Whangbo *et al.* have analyzed the superexchange interactions in $CaMn_2O_4$ on the basis of a molecular orbital dimer (MOD) approach [13]. They have considered six different superexchange paths and have identified the three most significant AFM exchange interactions, depicted in Fig. 8. The corresponding exchange integrals have been estimated on a relative scale as $J_1 : J_2 : J_3 = 0.40 : 1.0 : 0.72$. Their

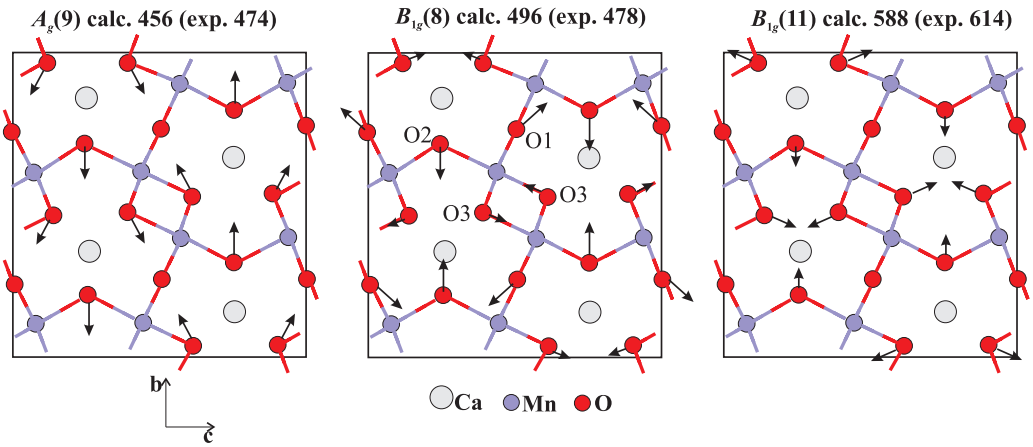

FIG. 7. (Color online) Calculated atomic displacement vectors for the three modes displaying anomalous softening below T_N. The inequivalent oxygen atoms are labeled.

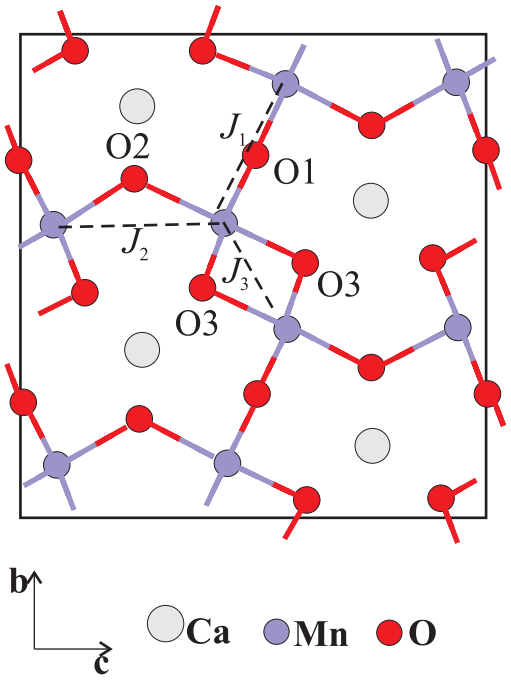

FIG. 8. (Color online) The most significant AFM interactions in $CaMn_2O_4$ according to Ref. [13]. The corresponding exchange integrals are indexed according to the oxygen atoms mediating the superexchange.

values on an absolute energy scale, however, could be reliably estimated on the basis of the simplest mean-field (MF) approach due to the relatively high spin, $S = 2$, of the Mn^{3+} ions. In the MF approximation, the Néel temperature is related to the nearest-neighbor exchange integrals by the equation $T_N = (1/3)S(S+1)\sum_i J_i$, which gives the values of three relevant J_i as reported in the second column of Table III.

According to a MOD, the three most important superexchange paths contain pairs of short (equatorial) Mn-O bonds sharing a common oxygen atom. The corresponding AFM coupling takes part between the singly occupied $3d(t_{2g})$ orbitals of Mn^{3+} ions through π overlap with the $2p$ orbitals of the mediating O^{2-} ions. The σ overlap between $3d(3z^2 - r^2)$ was found to be very weak due to the long apical Mn-O distances, while that between $3d(x^2 - y^2)$ does not lead to AFM interactions since the latter orbitals are not occupied.

By following the MOD approach, we will focus on the second derivatives of the exchange integrals with respect to the oxygen displacements. For this purpose, we will consider a Mn^{3+} dimer containing an intermediate oxygen atom in a general position, as shown in Fig. 9. It will be assumed, however, that at equilibrium, oxygen position $\alpha = \beta$ and $r_1 = r_2 \approx 1.9$ Å, which is the mean equatorial Mn-O distance. The corresponding angle $\theta = \alpha + \beta$ varies from 98° for Mn-O3-Mn to 135° for the Mn-O2-Mn dimer. Shown in Fig. 9 are also the active magnetic orbitals on Mn^{3+} ions, which couple through π overlap with the $2p$ oxygen orbitals. Note that the atomic orbitals are expressed in local coordinates. For the manganese ions, the x and y axes are, respectively, parallel and perpendicular to the Mn-O bonds. The x (y) axis for the oxygen atom is parallel (perpendicular) to the Mn-Mn

TABLE III. Estimated exchange integrals J_i, and their second derivatives J_s'' for symmetric and J_a'' for antisymmetric oxygen vibrations. The first column specifies the inequivalent oxygen atoms, which mediate the corresponding exchange interactions.

Oxygen atom	J_i (meV)	J_s'' (eV Å^{-2})	J_a'' (eV Å^{-2})
O1	1.80	0.064	–0.006
O2	4.50	0.050	–0.012
O3	3.24	0.126	–0.011

line. The z axis is common for all atoms and is perpendicular to the Mn-O-Mn plane. A small oxygen displacement along x represents an antistretching vibration, which preserves to a first approximation the angle θ and leads to an antiphase modulation of r_1 and r_2. An oxygen displacement along y corresponds to a symmetric stretching vibration, which modulates both the bond angle θ and the two Mn-O distances.

In the MOD approach, each pair $\mu\nu$ of magnetically interacting $3d$ orbitals gives an additive contribution to the exchange integral $J_{\mu\nu} = 2\sum t_{\mu\nu}^2/U$, where $t_{\mu\nu}$ is the hopping amplitude between orbitals μ and ν along a specific superexchange path, U is the effective Hubbard on-site repulsion, and the sum includes all possible superexchange paths between the two orbitals. Thus, for the two Mn xy orbitals, there are two connecting paths along the p_x and p_y oxygen orbitals, as shown in Fig. 9(a). By retaining only the lowest nonzero term in the perturbative expansion for $t_{\mu\nu}$, we obtain

$$t_{xy,xy} = -\frac{V_{pd\pi}(r_1)V_{pd\pi}(r_2)}{\Delta}\cos\theta, \tag{3}$$

where $\theta = \alpha + \beta$, $\Delta = E_{t_{2g}} - E_p$ is the difference between Mn t_{2g} and O $2p$ atomic orbital energies, and $V_{pd\pi}(r)$ is the off-diagonal Hamiltonian element corresponding to π bonding between the $2p$ and $3d$ orbital. The hopping amplitude between Mn xz orbitals is mediated by the oxygen p_z orbital, as seen in Fig. 9(b), and is independent on the Mn-O-Mn angle:

$$t_{xz,xz} = -\frac{V_{pd\pi}(r_1)V_{pd\pi}(r_2)}{\Delta}. \tag{4}$$

The Mn yz orbitals are of a δ character relative to the Mn-O bonds and do not couple through oxygen $2p$ orbitals. They could display some small direct overlap, which, however, is not modulated by the oxygen displacement and does not contribute to the observed frequency shifts.

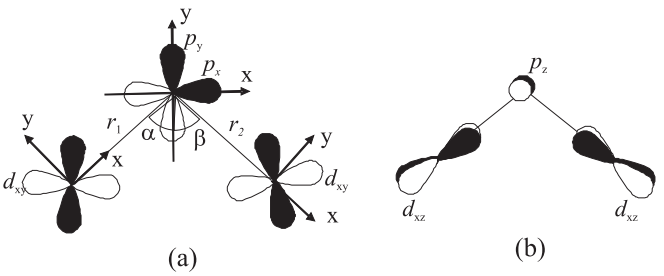

FIG. 9. Sketch of the relevant $3d$ orbitals, which are coupled by π overlap.

In the extended Huckel model (EHM) approach, the matrix element $V_{pd\pi}(r)$ is expressed through the π-overlap integral between the d and p wave functions as $\beta(E_{t_{2g}} + E_p)S_{pd\pi}(r)$, where β is a dimensionless constant. Therefore, the AFM exchange integral between the two Mn sites could be represented as

$$J = C S^2_{pd\pi}(r_1) S_{pd\pi}(r_2)^2 (1 + \cos^2\theta), \quad (5)$$

where the prefactor C includes all on-site quantities (Hubbard-U, atomic orbital energies) and does not depend on the bond lengths and bond angles. The overlap integral was evaluated for the optimized double-ζ atomic wave functions, reported in Ref. [13]. The coefficients C were fit for the superexchange paths containing the O1, O2, and O3 atoms in order to reproduce the MF values of J_i given in Table III.

On the basis of Eq. (5), we calculated the second derivatives of the exchange integral: $J''_s = \partial^2 J/\partial y^2$ for symmetric and $J''_a = \partial^2 J/\partial x^2$ for antisymmetric oxygen vibrations. The values obtained for the three inequivalent oxygen positions are summarized in Table III. The $B_{1g}(11)$ vibration (see Fig. 7) is comprised of symmetric vibrations of the O2 and O3 atoms only and, according to the positive sign of J''_s, is expected to experience softening below T_N. The temperature behavior of the other two modes shown in Fig. 7 is less evident since they contain both symmetric and antisymmetric components. However, the softening of these modes can be deduced by noticing that the negative J''_a for the antisymmetric vibrations, which tend to harden the mode frequency, are five to ten times weaker in absolute value than the corresponding positive contributions J''_s from the symmetric components of the atomic displacements.

The frequency softening for the three modes, estimated on the basis of Eq. (2), also corroborate well the experimentally observed values. At the lowest accessible temperature of 80 K, the mean-field estimate of the static magnetization gives $M \approx 1.9$, and correspondingly the nearest-neighbor spin-spin correlation function is $\langle S_i \cdot S_j \rangle \approx -3.6$. For the $B_{1g}(11)$ mode observed at 614 cm^{-1}, which involves predominately pure O3 symmetric vibration, the substitution of $J'' = 0.128$ eV Å^{-2} in Eq. (2) gives $\delta\omega \approx -9.7$ cm^{-1}. For the two lower frequency $B_{1g}(8)$ and $A_g(9)$ modes, assuming a dominant contribution from the O2 atom with $J'' \approx 0.05$ eV Å^{-2}, a frequency softening of $\delta\omega \approx -5.1$ cm^{-1} could be deduced, in fair agreement with the experiment.

V. SUMMARY AND CONCLUSIONS

We obtained polarized Raman spectra from oriented single crystals of $CaMn_2O_4$ (marokite) in all informative scattering configurations. The observed phonon lines follow the expected polarization selection rules for the $Pbcm$ space group and are classified unambiguously into irreducible representations.

The observed resonance enhancement of the Raman bands under 633 nm laser excitation has been associated with the 638 nm optical absorption band reported in Ref. [9].

Upon decreasing the temperature, most of the Raman modes follow the typical anharmonic frequency hardening. However, three of the modes—two B_{1g} and one A_g—display anomalous softening as the temperature drops below T_N. The first-principles DFT calculations of the lattice dynamics show that these modes involve almost pure oxygen vibrations within Mn-O-Mn planes. The molecular-orbital dimer approach predicts that the superexchange interactions between nearest-neighbor Mn sites contribute for softening of the symmetric oxygen vibrations below the Néel temperature and a much weaker, practically unobservable hardening of the antisymmetric vibrations. The theoretically estimated frequency softening is in good agreement with the observed experimental values and further validates the mechanism of frequency renormalization proposed by Granado *et al.* in the case of manganese perovskites.

ACKNOWLEDGMENTS

This work was supported in part by the State of Texas through the Texas Center for Superconductivity at the University of Houston and by the Science Fund of the University of Sofia through Contract No. 085/2014. M.V.A. thanks the Brazilian agency CAPES (Project No. BEX 7607-13-0) for financial support. D.Z.D. and V.G.I. are also supported by the Project INERA (GA316309) of the 7-th Framework Program of the European Union.

[1] D. K. Kim, P. Muralidharan, H.-W. Lee, R. Ruffo, Y. Yang, C. K. Chan, H. Peng, R. A. Huggins, and Y. Cui, Nano Lett. **8**, 3948 (2008).

[2] H. G. Geisber, W. T. Pennington, and J. W. Kolis, Acta Cryst. C **57**, 329 (2001).

[3] Z. Wang, S. K. Saxena, and J. J. Neumeier, J. Solid State Chem. **170**, 382 (2003).

[4] T. Yamanaka, A. Uchida, and Y. Nakamo, Am. Mineral. **93**, 1874 (2008).

[5] C. D. Ling, J. J. Neumeier, and D. N. Argyriou, J. Solid State Chem. **160**, 167 (2001).

[6] S. Zouari, L. Ranno, A. Cheikh-Rouhou, O. Isnard, M. Pernet, P. Wolfers, and P. Strobel, J. Alloys Compounds **353**, 5 (2003).

[7] B. D. White, C. A. M. dos Santos, J. A. Souza, K. J. McClellan, and J. J. Neumeier, J. Cryst. Growth **310**, 3325 (2008).

[8] B. D. White, J. A. Souza, C. Chiorescu, J. J. Neumeier, and J. L. Cohn, Phys. Rev. B **79**, 104427 (2009)

[9] X.-W. Wu, H.-X. Zhang, X.-J. Liu, and X.-G. Zhang, Chin. Phys. Lett. **28**, 107101 (2011).

[10] E. Granado, N. O. Moreno, A. García, J. A. Sanjurjo, C. Rettori, I. Torriani, S. B. Oseroff, J. J. Neumeier, K. J. McClellan, S.-W. Cheong, and Y. Tokura, Phys. Rev. B **58**, 11435 (1998).

[11] E. Granado, A. García, J. A. Sanjurjo, C. Rettori, I. Torriani, F. Prado, R. D. Sánchez, A. Caneiro, and S. B. Oseroff, Phys. Rev. B **60**, 11879 (1999).

[12] J. Laverdière, S. Jandl, A. A. Mukhin, V. Yu. Ivanov, V. G. Ivanov, and M. N. Iliev, Phys. Rev. B **73**, 214301 (2006).
[13] M.-H. Whangbo, H.-J. Koo, D. Dai, and D. Jung, Inorg. Chem. **41**, 5575 (2002).
[14] G. M. Sheldrick, Acta Cryst. A **64**, 112 (2008).
[15] P. Giannozzi, S. Baroni, N. Bonini, M. Calandra, R. Car, C. Cavazzoni, D. Ceresoli, G. L. Chiarotti, M. Cococcioni, I. Dabo, A. Dal Corso, S. de Gironcoli, S. Fabris, G. Fratesi, R. Gebauer, U. Gerstmann, C. Gougoussis, A. Kokalj, M. Lazzeri, L. Martin-Samos, N. Marzari, F. Mauri, R. Mazzarello, S. Paolini, A. Pasquarello, L. Paulatto, C. Sbraccia, S. Scandolo, G. Sclauzero, A. P. Seitsonen, A. Smogunov, P. Umari, and R. M. Wentzcovitch, J. Phys.: Condens. Matter **21**, 395502 (2009).
[16] E. Kroumova, M. I. Aroyo, J. M. Perez-Mato, A. Kirov, C. Capillas, S. Ivantchev, and H. Wondratschek, Phase Trans. **76**, 155 (2003); http://www.cryst.ehu.es/.
[17] I. P. Ipatova, A. A. Maradudin, and R. F. Wallis, Phys. Rev. **155**, 882 (1967).
[18] M. Balkanski, R. F. Wallis, and E. Haro, Phys. Rev. B **28**, 1928 (1983).